ACS Sustainable Chemistry & Engineering

pubs.acs.org/journal/ascecg

Research Article

Enhanced Formate Concentration via Alkaline CO_2 Electrolysis Using a Nickel Anode in a Zero−Gap Electrolyzer

Andreyna Ferreira Gamba,* Sergio Sanz,* Urbain Nzotcha, Hermann Tempel, and Rüdiger−A. Eichel

Cite This: ACS Sustainable Chem. Eng. 2026, 14, 1608−1619

ABSTRACT: The electrochemical reduction of CO_2 to formic acid is a promising route for decarbonizing the conventional industrial production of formic acid. Among the three most successful electrolyzers, the zero−gap (ZG) design stands out for its low cell complexity, making it particularly attractive for scalable applications. However, the low product concentration at the reactor outlet increases the cost of downstream purification processes, penalizing the ZG electrolyzer. This study addresses this technical challenge by using a ZG electrolyzer with an anionic exchange membrane (AEM) configuration, incorporating a PiperION AEM, a Bi_2O_3−coated gas diffusion electrode (GDE) as the cathode, and either a nickel mesh or IrO_2−coated GDE as the anode electrode. Surprisingly, the nickel mesh outperformed the IrO_2−coated GDE across the studied key performance indicators (KPs). At current densities of 50 and 100 mA cm^{-2}, the cell operated with faradaic efficiencies ranging from 94.24 to 75.50%, low energy consumption values between 2.69 and 4.63 kWh $kg^{-1}_{formate}$, and achieved the highest reported formate concentration (0.555 M) for a ZG cell design with an AEM configuration. Techno−economic analysis indicates a promising outlook for scalability using the presented ZG electrolyzer configuration with the nickel mesh.

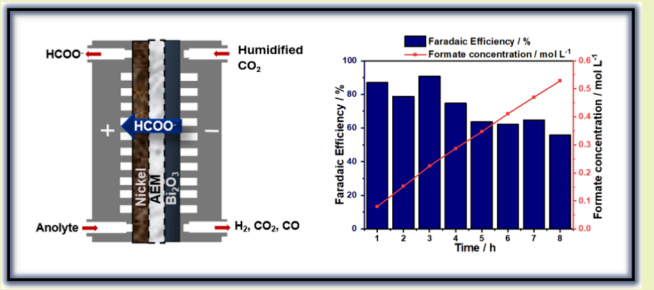

KEYWORDS: *CO_2 electroreduction, CO_2 utilization, formate production, zero−gap electrolyzer, anion exchange membrane, nickel catalyst*

1. INTRODUCTION

Since the start of the Industrial Revolution in the mid−18th century, global atmospheric carbon dioxide (CO_2) levels have increased by over 50%.[1] Climate change, triggered by high CO_2 concentration in the atmosphere, threatens the environment while straining the global economy and human society. Among the sectors targeted for decarbonization, the industrial sector is particularly significant, especially due to its potential for integrating carbon capture and utilization (CCU) technologies.[2−4] In this context, the electrochemical reduction of CO_2 (eCO_2R) has emerged as a promising strategy to convert surplus CO_2 into sustainable fuels and value−added chemicals.[5] Moreover, it can be powered by renewable energy sources (wind and solar), thereby facilitating the transition of the synthetic processes toward a circular carbon economy.[6−8] CO_2 electrolysis generates a wide range of products, including carbon monoxide, methanol, ethanol, and formic acid.[3,9] Compared to other eCO_2R products, formic acid has the potential for industrial−scale production and economic competitiveness with the current market price of ∼ 0.6 \$ kg^{-1}. Formic acid finds application in multiple fields, such as textile and leather processing, as well as in formulations for preservatives, fertilizers, antifreeze, and heat-transfer.[10,11] Additional applications, currently under investigation, include its use in direct formic acid fuel cells, syngas storage medium, as a chemical reagent in organic processes, and a feedstock for bioprocesses.[12,13]

To achieve industrial applicability, technological improvements in components (*e.g.*, catalysts, electrodes, membranes, electrolytes, solvents) must progress alongside the design and scaling−up of flow cell electrolyzers.[5,13] The three most common electrolyzer configurations investigated for eCO_2R−to−HCOOH are the zero−gap (ZG), dual−flow (DF), and direct formic acid production (DFAP) systems (Figure 1).[4] The ZG design is the simplest configuration, with cathode, membrane, and anode assembled—minimizing ohmic losses and enabling a compact architecture.[14] The DF electrolyzer features separate anolyte and catholyte compartments, allowing control over electrolyte composition and potential operation at higher current densities.[4] The DFAP system employs a three−compartment configuration with a solid-state electrolyte (SSE)

Received: October 15, 2025
Revised: December 30, 2025
Accepted: December 31, 2025
Published: January 12, 2026

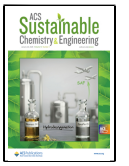

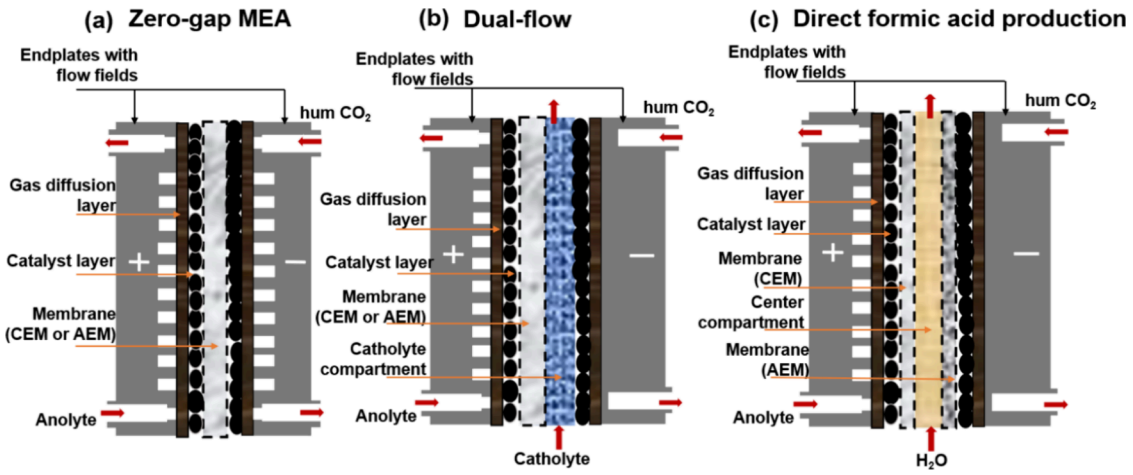

Figure 1. Schematic of the most common electrolyzers: (a) zero−gap (ZG), (b) dual flow (DF), and (c) direct formic acid production (DFAP).

between a cation exchange membrane (CEM) and an anion exchange membrane (AEM), enabling the direct production of formic acid.[15−17] While DF systems enable electrolyte management and DFAP design achieves higher product concentrations, the simplicity of the ZG design makes it particularly attractive for economies of scale.[4,6,13,18] Although not an eCO_2R−to−$HCOO^-$ electrolyzer, bicarbonate-reduction reactors have demonstrated excellent performance and also achieve high formate concentrations.[19−21]

Typically, the ZG electrolyzer consists of an anode performing the oxygen evolution reaction (OER) in an aqueous electrolyte, a cathode supplied with humidified CO_2, and an ion exchange membrane—either cationic (CEM) or anionic (AEM)—separating the two compartments.[14] The anolyte plays a crucial role in facilitating charge transfer between the electrodes and the catalyst during CO_2 reduction, while also enhancing ionic conductivity and suppressing the hydrogen evolution reaction (HER).[22]

The ion exchange membrane plays a decisive role in this design's performance, with the CEM ensuring that product formation is primarily released in the cathodic compartment. Although humidified CO_2 enhances formate concentration, the system's operation is undermined by salt precipitation on the cathode that progressively obstructs the flow pathways. Adding catholyte circumvents this problem, but dilutes the product and promotes the HER, particularly at high current densities. The use of AEM has been successfully demonstrated in recent studies using humidified CO_2 in the cathodic compartment and an anolyte solution based on either $KHCO_3$ or KOH. Compared to CEM−based set−ups, this configuration enables longer−term operation while achieving higher current densities with good selectivity toward formate. Introducing a perforated CEM between the anode and AEM (forward bias bipolar membrane) results in a concentration of 0.25 mol L^{-1} at 300 mA cm^{-2}, with energy consumption of 2.91 kWh kg^{-1} when using hydrogen oxidation in the anode.[23] However, this configuration increases system complexity, particularly concerning scalability, due to the technical challenges of integrating an additional perforated CEM.

Bismuth−based catalysts demonstrate high activity and selectivity toward eCO_2R to formate while being abundant and environmentally benign. As a non−noble metal, it contributes to reducing overall production costs.[13] The OER is commonly used as the anodic reaction. It is typically catalyzed by iridium−based electrodes (e.g., IrO_2)——a rare and expensive noble metal——which significantly influences the overall reaction cell voltage and energy efficiency.[24,25] Despite its good performance, the high cost of iridium poses significant challenges to economic viability, particularly in terms of scalability.[26] Among the promising alternatives, nickel is an active OER catalyst, mostly studied in alkaline water electrolysis, offering good performance and stability.[27] Although less studied, nickel can serve as a low−cost anode when the OER is used as a counter reaction in CO_2 electroreduction cells, especially under alkaline conditions. In the eCO_2R to formate using a zero−gap electrolyzer with a single membrane configuration, although Ir−based catalysts are still dominant for the OER, two examples are reported with nickel catalyst: one employing a CEM and the other an AEM (Table S1, entries 3, 9).

Herein, we developed a customized zero−gap electrolyzer——fabricated in house——incorporating a PiperION AEM, a Bi_2O_3−coated GDE as the cathode, and either a nickel mesh or IrO_2−coated GDE as the anode for catalyzing the OER. When the nickel mesh was used as the anode, this configuration enabled eCO_2R to formate with a concentration of 0.555 M——the highest reported to date for a ZG cell in an AEM configuration. Additionally, the influence of the anodic electrolyte (NaOH, KOH, and CsOH), pH (OH^- vs. HCO_3^-), and PiperION membrane thickness (40—80 μm) was investigated to assess their impact on key performance indicators. Hence, this study presents an economical improvement using a zero-gap AEM electrolyzer by replacing iridium with low-cost nickel mesh, resulting in lower process costs and improved key performance indicators (KPIs), as demonstrated by techno-economic analysis (TEA). Although the product obtained under the studied conditions is diluted potassium formate, the ultimate target product is commercial-grade formic acid (>85 wt %). To this end, downstream processes (acidification, extraction, and distillation) must be implemented, as detailed in section 3.4 (techno-economic studies).

2. EXPERIMENTAL SECTION

2.1. Materials

Chemical reagents were used as received from commercial suppliers. Nickel mesh with a wire diameter of 0.16 mm (Haver & Boecker OHG, Germany), Freudenberg E20H GDL (Quintech, Germany), PiperION AEM (Versogen, USA) of different thicknesses (60 μm, 40

https://doi.org/10.1021/acssuschemeng.5c11134
ACS Sustainable Chem. Eng. 2026, 14, 1608−1619

μm, and 80 μm), IrO_2–based GDE (Dioxide Materials, USA), and Bi_2O_3–based GDE (Dioxide Materials, USA) were commercially available. The zero–gap electrolyzer, which provides a 9.0 cm^2 geometric active area was manufactured in–house (Figure S1).

2.2. Zero–Gap (ZG) Electrolyzer Setup

The zero–gap (ZG) electrolyzer comprises two titanium end plates with serpentine flow paths that also serve as anode and cathode current collectors (not additionally metal–coated for conductivity), two 25 μm–thick PTFE gaskets, a commercial Bi_2O_3 GDE as the cathode, a PiperION AEM with a thickness ranging from 40 to 80 μm, and an anode, which can be either a commercial IrO_2 GDE or a nickel mesh supported on commercial Freudenberg E20H GDL. Figure S2 shows the ZG configuration using nickel as an anode. Figure S3 depicts the anodic compartment, featuring the nickel mesh supported on Freudenberg E20H GDL, mounted on the anodic current collector containing a serpentine flow field. All components (cathode, membrane, and anode) were assembled by applying torques of 1.5 and 2.0 N m.

2.3. Electrochemical Measurements and Analytical Methods

After assembly, the cell was pre–conditioned using 1 M KOH anolyte solution via chronopotentiometry (CP) at 0.45 A, until a stable potential value was reached (~1.5 h). Four distinct blocks of experiments were conducted in this study to evaluate (a) the type of anodic material (iridium vs nickel), (b) the stability of the measured KPIs over time using the investigated iridium– and nickel–based electrodes, (c) the anolyte composition, and (d) the AEM thickness——both using a nickel mesh——on the studied KPIs. The first block evaluated the effect of IrO_2–based and nickel mesh anodes on the electrolyzer performance using CP at different current densities (50, 100, and 200 mA cm^{-2}) for 2 h. The experiments were conducted using KOH as an anolyte at two concentrations: 1 and 2 M. Additionally, a mechanistic study was carried out to evaluate the formate oxidation reaction (FOR) using nickel mesh and IrO_2–based GDE. The study was performed by adding 0.44 M KCOOH to the anolyte (1 M KOH) and applying a current density of 100 mA cm^{-2}, while feeding Ar to the cathode instead of CO_2 for 2 h. The second block examined the stability of the electrolyzer using the nickel mesh and the IrO_2–based anodes, carrying out continuous electrolysis (CP) at 50 mA cm^{-2} over an extended operation time (4—8.7 h) using 2 M KOH. The third block of experiments investigated the impact of the anolyte composition (NaOH, KOH, CsOH, and $KHCO_3$) using CP at 50 mA cm^{-2} for 2 h, using the nickel mesh as an anode. Initially, the cation effect was assessed by comparing 1 M CsOH, KOH, and NaOH as anolytes. Subsequently, the anion effect, which also influences the reaction pH, was investigated by comparing 1 M KOH, 1 M $KHCO_3$, and K_2SO_4 under the same conditions. Finally, the fourth block of measurements assessed the influence of membrane thickness (40—80 μm) on the electrolyzer performance over 2 h operation, using previously optimized conditions: 1 M KOH as the anolyte and a nickel mesh anode.

Humidified CO_2 was supplied in excess to the cathode at a constant flow rate of 40.0 sccm for current densities of 50 and 100 mA cm^{-2}, and 80 sccm for 200 mA cm^{-2}. Humidification was achieved using a water–filled bubbler before entering the electrolyzer, as illustrated in Figure S4. The anode was supplied with argon at a flow rate of 40 sccm to maintain a controlled, inert, and measurable environment at the anode. The anolyte was introduced and recirculated at

100 mL min^{-1} using a peristaltic pump (MasterFlex 78018–42 Dual Channel). Desired gas flow rates were introduced in the electrolyzer using a mass flow control (MFC – EL–Flow Prestige, Bronkhorst) and quantified via a drum gas counter (TG0.5–PVC–PVC, Ritter, Germany) using AMR Win Control Software for data acquisition.

Electrochemical measurements were conducted using an electrochemical station (Metrohm Potentiostat, PGSTAT302N) coupled to a high–current booster (Metrohm, Booster10A). It was used in a four–electrode mode: working electrode (WE), counter electrode (CE), reference electrode (RE), and working sense (S). To evaluate the electrochemical behavior, chronopotentiometry (CP) was conducted at different current densities (50—200 mA cm^{-2}). The gaseous products formed in the electrolysis were collected at time intervals and analyzed by Gas Chromatography (GC, ThermoFischer P–GC–TCD Duplex 3). Aliquots (0.5 mL) of the recirculated anolyte were collected from the anolyte reservoir throughout the reaction to determine formate concentration by ion chromatography (IC, Sykam Ion Exclusion Chromatography S155). Samples were taken every 20 min, except during long-term stability tests, in which aliquots were collected every 60 min. Experimental data are reported as the average of duplicate measurements. Utilizing the CP experimental data and the quantified flow rates, together with the product concentration calculated by GC and IC, the KPIs were calculated using eqs 1-3.

Faradaic Efficiency (FE – %) of formate:

$$\mathrm{FE}_{\mathrm{formate}}(\%) = \frac{n_{\mathrm{formate}} \times z \times F}{j \times A \times t} \times 100 \quad (1)$$

Faradaic Efficiency (FE – %) of gaseous products (H_2 and CO):

$$\mathrm{FE}_{\mathrm{CO/H2}}(\%) = \frac{\dot{n}_{H2/CO} \times z \times F}{j \times A} \times 100 \quad (2)$$

Energy consumption (EC – kWh kg^{-1}):

$$\mathrm{EC} = \frac{U_{\mathrm{cell}} \times q}{m_{\mathrm{formate}}} \quad (3)$$

Where n refers the number of moles of formate produced, $\dot{n}$ denotes the molar flow, z denotes the stoichiometric number of electrons required to form the product, F refers to the Faraday constant (96485 C mol^{-1}), j denotes the current density, A refers to the geometric active electrode area, t denotes the elapsed time, U_{cell} refers to the cell potential, q denotes the electric charge, and m_{formate} refers to the mass of formate produced.

2.4. *Post Mortem* Characterization

To examine structural changes in the electrodes, *post mortem* characterizations were carried out after applying 200 mA cm^{-2} for 2 h. Blank analyses were conducted before the reaction to establish a baseline for comparison. To compare the morphology, Scanning Electron Microscopy (SEM, model FEI Quanta FEG 650; 20 kV acceleration voltage; 3 nm spot) was performed with element mapping using coupled Energy Dispersive X–Ray Spectroscopy (EDS; 20 kV acceleration voltage; 5 nm spot). Superficial composition was determined by X–ray photoelectron spectroscopy (XPS, model PHI5000 VersaProbe II, ULVAC–Phi Inc., USA) with a monochromatic Al–Kα radiation (1.486 keV; X–Ray Setting: 50 W, 15 kV, 200 μm spot). Charge correction was done by setting the main component of the C 1s spectra to 285 or 284.5 eV for sp^3 and sp^2 carbon, respectively, and the satellite peaks (SP) were considered in the composition percentage.[28] Inductively Coupled Plasma Mass Spectrometry (ICP–MS) was used to assess whether nickel mesh was leaching. To identify crystalline phases, X–ray diffraction (XRD) measurements were carried out using Cu Kα radiation (XRD, Panalytical Empyrean DY 2785).

3. DISCUSSION OF RESULTS

Due to the high cost, scarcity, and supply risk of iridium, significant research is underway to investigate the use of cheap and abundant catalysts with non–noble metals for electrolytic reactions, particularly in the OER. In alkaline media, transition metal oxides based on nickel, iron, cobalt, and manganese, and their combinations have demonstrated promising activity and stability, offering viable alternatives to IrO_2.[29] Additionally, spinel and perovskite materials, known for their structure tunability, are also being investigated.[30] In the context of CO_2

https://doi.org/10.1021/acssuschemeng.5c11134
ACS Sustainable Chem. Eng. 2026, 14, 1608–1619

Table 1. (Left) Comparative Results and Standard Deviation (SD) of KPIs for Anodic IrO_2–Based GDE and Nickel Mesh in the ECO_2R–to–Formate Using a ZG Electrolyzer with an AEM at Different Current Densities[a]

entry	anode	anolyte KOH	current density [mA cm^{-2}]	EC [kWh kg^{-1}]	cell voltage [V]	FE [%]	accumulated formate [M]
1	Ni mesh	1 M	50	2.69 ± 0.00	2.32 ± 0.02	94.24 ± 1.73	0.163 ± 0.000
2	Ni mesh	1 M	100	4.63 ± 0.09	2.64 ± 0.07	75.50 ± 14.25	0.198 ± 0.006
3	Ni mesh	1 M	200	16.73 ± 1.12	3.26 ± 0.20	12.60 ± 3.02	0.099 ± 0.019
4	Ni mesh	2 M	50	2.93 ± 0.22	2.13 ± 0.01	86.17 ± 9.40	0.146 ± 0.008
5	Ni mesh	2 M	100	9.64 ± 0.25	2.69 ± 0.02	28.04 ± 0.78	0.106 ± 0.013
6	Ni mesh	2 M	200	36.72 ± 2.38	2.67 ± 0.02	8.13 ± 0.21	0.054 ± 0.006
7	IrO_2	1 M	50	4.36 ± 0.25	2.12 ± 0.04	57.36 ± 0.95	0.101 ± 0.015
8	IrO_2	1 M	100	7.24 ± 9.13	2.68 ± 0.08	12.11 ± 4.87	0.049 ± 0.017
9	IrO_2	1 M	200	71.60 ± 33.87	3.01 ± 0.08	0.47 ± 0.63	0.008 ± 0.001
10	IrO_2	2 M	50	5.59 ± 1.14	2.20 ± 0.02	43.74 ± 6.62	0.079 ± 0.015
11	IrO_2	2 M	100	13.72 ± 4.22	2.51 ± 0.06	21.24 ± 7.45	0.080 ± 0.055
12	IrO_2	2 M	200	292.56 ± 93.38	3.040 ± 0.07	1.30 ± 0.89	0.012 ± 0.004

[a]Reaction setup: Bi_2O_3–GDE cathode, 60 μm PiperION AEM, humidified CO_2 flow (40 mL min^{-1}), recirculation of anolyte (KOH) at 100 mL min^{-1} over 2 h.

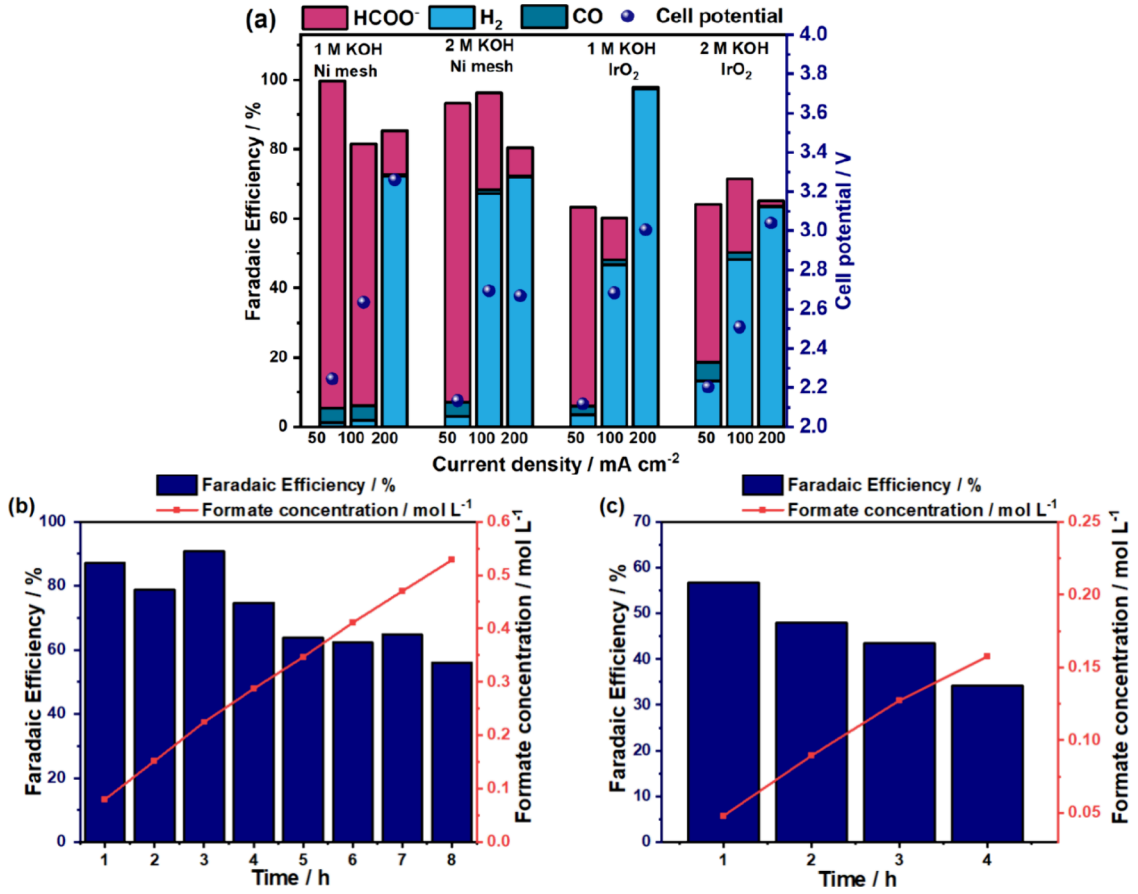

Figure 2. (a) Plot of the average faradaic efficiencies (%) and cell potential (V) vs current densities based on the data presented in Table 1. Reaction conditions are as specified in Table 1. Plot of the average faradaic efficiencies (%) and formate concentration (M) vs time of reaction (h) using anodic (b) nickel mesh and (c) IrO_2–based GDE. Reaction set–up: Bi_2O_3–GDE cathode, 60 μm PiperION AEM, 40 mL min^{-1} of humidified CO_2 flow, and recirculation of 2 M KOH as anolyte at 100 mL min^{-1}. Reaction time: 8.7 and 4 h, for (a) and (b), respectively.

electrolysis, nickel–based materials such as nickel mesh, nickel foam, and nickel–iron (oxy)hydroxides are gaining momentum under alkaline conditions.[31−34] These developments are essential to enhance the scalability of electrolyzers by reducing dependence on scarce noble metals. While economies of scale have already been achieved in water electrolysis, the eCO_2R to value–added products is still in its early stages, beginning with demonstration–scale reactors, particularly with two–electron products, such as CO and HCOOH. A recent techno–economic analysis of the eCO_2R–to–HCOOH process has shown the potential for this route to compete economically with the current industrial synthetic processes.[4] Among typical electrolyzer configurations, the ZG reactor is the most suitable for scalability due to its simple design. However, it faces economic drawbacks related to the high cost of downstream

https://doi.org/10.1021/acssuschemeng.5c11134
ACS Sustainable Chem. Eng. 2026, 14, 1608−1619

processing associated with the low product concentration in the reactor outlet.

Our interest in using a ZG electrolyzer with an AEM configuration under alkaline conditions focuses on addressing two major limitations of this design for the eCO_2R–to–formate: the reliance on IrO_2 as a catalyst for the OER and the low concentration of the formate product. In the following sections, we investigate (a) the replacement of IrO_2 with nickel mesh as active material for the OER, (b) strategies to optimize product concentration, and (c) the impact of the electrolyte composition and AEM thickness on KPIs with the configuration using the nickel mesh, which as we anticipate, demonstrates superior performance compared to the IrO_2 catalyst.

3.1. Comparison of the ZG Electrolyzer Performance Using IrO_2–Based GDE and Nickel Mesh Anodes, and Optimization of Formate Concentration

The principal motivation behind this study is to evaluate the feasibility of replacing IrO_2 with nickel mesh as an anode material. In the first testing phase, specific KPIs were monitored with the two anodes using CP measurements at current densities of 50, 100, and 200 mA cm^{-2}. Measurements were conducted using 1 and 2 M KOH, as nickel exhibits enhanced performance in alkaline conditions. Calculated KPIs included energy consumption, faradaic efficiency, and accumulated formate concentration in the anolyte container due to anolyte recirculation.

Table 1 summarizes the results for the configurations studied: an IrO_2–based GDE and a nickel mesh anode, each tested with two different KOH anolyte concentrations at various current densities. Optimal energy consumption and faradaic efficiency were achieved at 50 mA cm^{-2} with nickel mesh in both 1 and 2 M KOH. Average faradaic efficiencies over 2 h exceeded 86%, with EC values of 2.69 and 2.93 kWh kg^{-1} for 1 and 2 M KOH, respectively (Table 1, entries 1 and 4). As the current density increased to 100 mA cm^{-2}, a higher formate oxidation at the anode is observed (Figure 2a). Nevertheless, the cell maintains stable with faradaic efficiency of 75.50%, an EC of 4.63 kWh kg^{-1}, and an accumulated formate concentration of 0.198 M (Table 1, entry 2).

At 200 mA cm^{-2}, the cell primarily produces hydrogen, while formate accounts for only 12.60 and 8.13% of FE to formate, for 1 and 2 M KOH, respectively (Table 1, entries 3 and 6). The increased HER at higher current densities and KOH concentration can be attributed to the increased water flux (j_{H2O}) toward the cathode. In this ZG cell configuration, j_{H2O} is dominated by the electro–osmotic drag (EOD), as water molecules are transported along with the flux of K^+ ions (j_{K+}) across the AEM, expressed as $j_{H2O} = \xi \cdot j_{K+}$. Here, the EOD coefficient (ξ) represents the number of water molecules transported per K^+ ion across the AEM under the electric field and is determined by the hydration coordination sphere——typically three water molecules for each K^+ ion——and the applied current density that drives K^+ transport through the membrane.[35−37] Although an ideal AEM should be anion–selective and impermeable to cations, cation crossover from anode to cathode occurs in ZG cells, increasing water transport. Permselectivity is further reduced under high electrolyte concentrations, as in the present study with 1 M KOH, due to the Donnan exclusion effect.[36] The highest hydrogen evolution, observed at 200 mA cm^{-2} and 2 M KOH for both anode configurations (Figure 2a), is consistent with the increased water supply to the cathode.[37]

Compared to the Ni mesh, the IrO_2–based anode is detrimental to the eCO_2R–to–formate in this cell configuration at all current densities, due to its lower faradaic efficiencies and higher energy consumption (Table 1, Figure 2a). The best performance of IrO_2 is observed at 50 mA cm^{-2}, with faradaic efficiencies of 57.36% and 43.74% for 1 and 2 M KOH, respectively (Table 1, entries 7 and 10). As shown in Figure 2a, FOR and HER are more pronounced when using the IrO_2–based anode.

In ZG electrolyzers with an AEM configuration, formate exits through the anode, and the average FE falls below 100% due to partial oxidation of formate, a process that becomes more pronounced at higher current densities (Figure S5–S6).[38−40] A mechanistic study was conducted to explain the superior performance of Ni mesh compared to IrO_2 in CO_2 electrolysis by investigating the FOR at the anode. FOR was evaluated by introducing 0.44 M of potassium formate into the anolyte (1 M KOH), while Ar was fed to the cathode. This setup eliminates the formation and product crossover from CO_2 electrolysis, enabling a direct assessment of FOR. CP measurements at 100 mA cm^{-2} showed that 11% of the formate was consumed by the IrO_2–based anode within 2 h (Figure S7b), whereas only 3.6% was consumed by the nickel mesh (Figure S7a). These results indicate that the FOR is more pronounced on IrO_2–based GDE than on nickel mesh, explaining the lower apparent FOR selectivity observed with the Ni mesh during CO_2 electrolysis. These findings are consistent with the trends reported in Table 1, Figure 2, and Figures S5–S6. Previous results indicated that the nickel mesh delivers the best KPIs at a current density of 50 mA cm^{-2} in 1 M KOH (Table 1, entry 1), achieving an accumulated formate concentration of 0.163 M after a 2h. For long measurement durations, FOR became predominant after 4 h for the nickel mesh anode (Figure S8a) and after 3 h for the Ir–based anode (Figure S8b).

To assess the stability of the electrolyzer using the nickel mesh and the IrO_2–based anodes, CP experiments with 2 M KOH were conducted at 50 mA cm^{-2}. These tests aimed to optimize the formate accumulation in the anodic reservoir using nickel mesh (Figure 2b) and IrO_2–based anode (Figure 2c). An accumulated formate concentration of 0.555 M was achieved when the nickel mesh was utilized. This represents a highly energy–efficient process (3.48 kWh kg^{-1}) and the highest formate concentration reported to date for a ZG electrolyzer in an AEM configuration, surpassing the 0.25 M benchmark previously achieved using a forward–bias bipolar membrane (BPM) with a perforated CEM (Table S1, entry 12).[23]

Under these optimized conditions, the formate concentration of 0.555 M is reached after 8.7 h. After this period, the anolyte should be replaced with a fresh 2 M KOH reservoir to initiate a new operating cycle. In contrast, the IrO_2–based GDE reaches saturation at 0.158 M after 4 h, with a drop of faradaic efficiency to 34.17%. Since the anolyte is recirculated and the quantification refers to the accumulated formate, this observation indicates that, after 4 h, the FOR dominates, and most of the formate produced at the cathode is being oxidized at the anode. The optimization process with the IrO_2–based anode would take 4 h, achieving an accumulated formate concentration of 0.158 M with an average energy consumption of 5.13 kWh kg^{-1} and faradaic efficiencies between 34.17%

https://doi.org/10.1021/acssuschemeng.5c11134
ACS Sustainable Chem. Eng. 2026, 14, 1608−1619

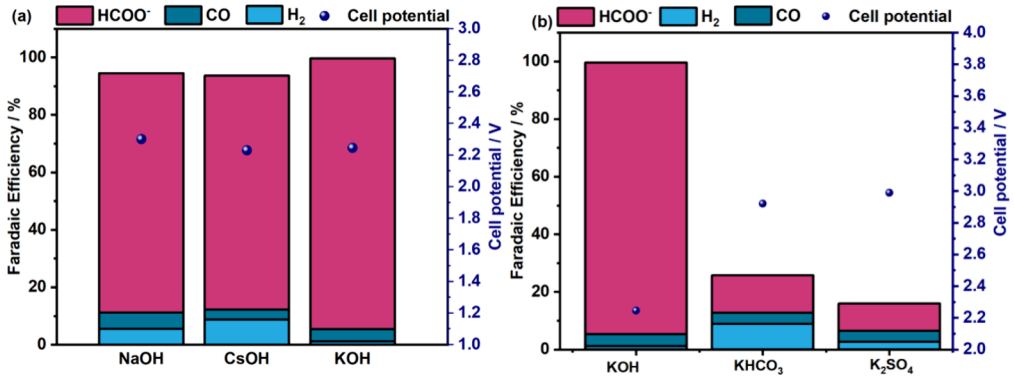

Figure 3. (a) Average faradaic efficiencies (%) versus different anolyte contents (NaOH, CsOH, and KOH) and cell potential (V) during CO_2 electrolysis. (b) Average faradaic efficiencies (%) versus different anolyte contents (KOH, $KHCO_3$, and K_2SO_4) and cell potential (V) during CO_2 electrolysis. Reaction conditions: anodic nickel mesh, cathodic Bi_2O_3–based GDE, 60 μm PiperION membrane, 50 mA cm^{-2} of current density, 40 sccm of CO_2 flow, 100 mL min^{-1} of anolyte flow in recirculation mode, and 2 h reaction.

and 56.67%. These results demonstrate that using a nickel mesh with the investigated electrolyzer configuration under alkaline conditions achieves the highest reported formate concentration, while leveraging its abundance, cost–effectiveness, and its favorable preference for the OER over the FOR in the investigated time.

3.2. Effect of Different Anolytes on the ZG Electrolyzer Performance

Using alkaline anolytes in the anodic compartment lowers the oxygen evolution potential (OEP), thereby reducing the energy demand for the OER and improving the overall energy efficiency of the electrolytic process. In the context of cathodic eCO_2R, the effect of cations in the catalytic reaction remains debated, with multiple theories proposed.[41] These include their role in regulating local pH and modifying local electrostatics—where cations accumulate at the outer Helmholtz plane (OHP), altering the electric field and stabilizing key reaction intermediates, such as adsorbed CO_2.[42] In a ZG electrolyzer equipped with an AEM, cations from the anolyte can still migrate toward the cathode under the influence of the electric field, carrying water molecules with them.[35,36] This process, known as electro–osmotic drag, is influenced not only by the electric field but also by the type of cation used in the anolyte. Smaller cations, such as Na^+, have a higher hydration number and thus transport more water molecules compared to larger cations like Cs^+.

To investigate the influence of different anolytes on the electrolyzer performance, CP experiments were conducted to evaluate both faradaic efficiency and formate concentration. The nickel mesh was selected as the anode, due to its enhanced performance. The rest of the cell configuration comprised a cathodic Bi_2O_3–based GDE and a 60 μm PiperION membrane. The cell operated at 50 mA cm^{-2}, a CO_2 flow rate of 40 sccm, and at 100 mL min^{-1} of anolyte flow in a recirculation mode over 2 h.

Three different anolytes——NaOH, KOH, and CsOH——were utilized to compare the cationic effect in the eCO_2R–to–formate. All tested anolytes demonstrated high selectivity to formate production, achieving high faradaic efficiencies (Figure 3a), similar cell potentials, and energy consumption (Table S2). Although Cs^+ possesses the largest ionic radius and the lowest hydration number among the cations tested—factors that contribute to a reduced water flux across the AEM toward the cathode—the highest selectivity was observed with K^+, which exhibited the lowest contribution to the HER. In general, these effects become more pronounced at high current densities due to the influence of the electric potential in the electro–osmotic drag and the Donnan exclusion effect.[43−45] At lower current densities, KOH tends to perform comparably to, or even better than, CsOH.[41,42,46]

Previously, the effect of different cations was evaluated under alkaline conditions by maintaining OH^- as the counteranion. Conversely, to study the influence of anions, K^+ was held constant while the anion species varied. $KHCO_3$, KOH, and K_2SO_4 were used as anolytes in these experiments, altering the local pH of both half reactions and, hence, their potential (eqs 4-6) and the overall energy efficiency of the electrolytic process.[47,24]

Anode:

$$2H_2O \rightarrow O_2 + 4H^+ + 4e^- E^0 = +1.23 (vs.\ SHE) \quad (4)$$

$$4OH^- \rightarrow O_2 + 2H_2O + 4e^- E^0 = +0.40 (vs.\ SHE) \quad (5)$$

Cathode:

$$CO_2 + H_2O + 2e^- \rightarrow HCOO^- + OH^- E^0 = -0.48 (vs.\ SHE) \quad (6)$$

The measured pH in the anolyte reservoir was ~ 8 with 1 M $KHCO_3$, ~ 14 with 1 M KOH, and ~ 7 with 1 M K_2SO_4. Moreover, it is well established that nickel exhibits superior catalytic performance under alkaline conditions.[48] On the cathodic site, the performance of the Bi_2O_3–based cathode toward the eCO_2R is enhanced under alkaline conditions due to the suppression of the HER.[36] Regardless of the anion, the HER remains consistently low, indicating comparable selectivity toward the eCO_2RR (Figure 3b, Table S2). However, when $KHCO_3$ and K_2SO_4 are used as anolytes, FOR at the anode becomes significantly more pronounced, resulting in a low performance. This suggests that on the investigated nickel mesh anode, the OER is less favorable under neutral conditions due to increased competition with the FOR. Hence, employing an alkaline medium is necessary in the studied electrolyzer configuration to both thermodynamically and kinetically promote the OER on the nickel anode, in line with reports on water electrolysis.[38,39,49,50]

https://doi.org/10.1021/acssuschemeng.5c11134
ACS Sustainable Chem. Eng. 2026, 14, 1608−1619

The average cell potential, and particularly the energy consumption, were optimized when using 1 M KOH (2.25 V; 2.69 kWh kg^{-1}), compared to $KHCO_3$ (2.92 V; 25.80 kWh kg^{-1}) and K_2SO_4 (2.99 V; 22.03 kWh kg^{-1}) (Figure 3b, Table S2). In terms of formate production, KOH yielded the highest concentration (0.163 M), given the low rate of formate oxidation. This was followed by $KHCO_3$ (0.115 M), and K_2SO_4(0.024 M) (Table S2).

3.3. Effect of Membrane Thickness on the ZG Electrolyzer Performance

The final parameter evaluated was the impact of membrane thickness on the performance of the electrolyzer. In this study, PiperION membranes——composed of a functionalized poly(aryl piperidinium) polymer——were evaluated. Variations in membrane thickness were expected to influence the efficiency of formate production. The nickel mesh was selected as the anode while the rest of the cell configuration comprised a cathodic Bi_2O_3–based GDE and a PiperION membrane with thicknesses ranging from 40 to 80 μm. The electrolyzer operated in a CP mode at current densities of 50, 100, and 200 mA cm^{-2}. A continuous CO_2 flow rate (40 sccm) was supplied to the cathode, while 1 M KOH was used as anolyte, recirculated at 100 mL min^{-1} over 2 h.

The medium–thick membrane (60 μm) promotes the highest selectivity toward formate production (Figure 4) and

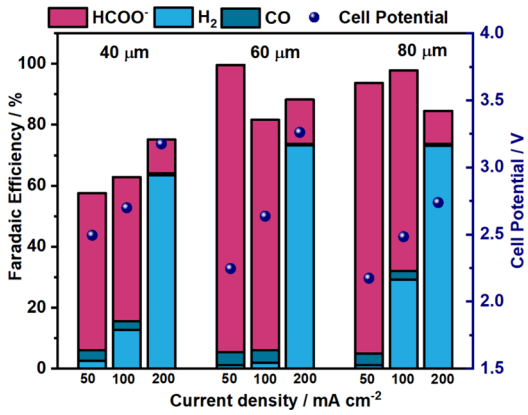

Figure 4. Average faradaic efficiencies (%) and cell potentials (V) at different current densities during CO_2 electrolysis using PiperION membranes of various thicknesses (40, 60, and 80 μm). Reaction conditions: anodic nickel mesh, cathodic Bi_2O_3–based GDE, 40 sccm of CO_2 flow, 100 mL min^{-1} anolyte flow of 1 M KOH in recirculation mode over 2 h.

the lowest energy consumption across all current densities (2.69 and 4.63 kWh kg^{-1} at 50 and 100 mA cm^{-2}, respectively; Table S3). Enhanced formate selectivity was only observed in the thicker and thinner membranes at 50 mA cm^{-2}, with superior cell performance with the 80 μm membrane (88.79% FE, 3.14 kWh kg^{-1}) compared to the 40 μm (51.40% FE, 6.09 kWh kg^{-1}) (Figure 4, Table S3). At 200 mA cm^{-2}, all membrane thicknesses predominantly favored HER, which is attributed to the increased water flow to the cathode at higher current densities.[45,51] A similar trend was recently reported using a MEA electrolyzer with PiperION membranes of various thicknesses under different current densities.[52] The ZG electrolyzer operates optimally with the 60 μm PiperION membrane at 50 and 100 mA cm^{-2}, by regulating the water diffusion to the cathode and minimizing FOR at the anode. However, while the thicker membrane (80 μm) regulates FOR at the anode comparable to the 60 μm membrane at the studied current densities, it fails to suppress HER at the cathode at 100 mA cm^{-2}, contradicting our initial assumptions and literature reports.[45,53] The 40 μm membrane neither controls water diffusion nor formate migration across it.

3.4. *Post Mortem* Characterization

Scanning Electron Microscopy (SEM) was used to assess GDE structural changes after electrolysis. Evaluation of the GDE before eCO_2R revealed white, spherical nanoparticle agglomerates (Figure 5b) that were homogeneously dispersed (Figure 5a). These agglomerates were identified by Energy Dispersive X–Ray Spectroscopy (EDS) as bismuth nanoparticles. After 2 h of electrolysis at 200 mA cm^{-2}, a crystalline product with defined edges (Figures 5c—d) appears on the surface of the GDE, identified as potassium by EDS mapping analysis (Figure S9).

This result indicates a significant potassium migration from the anode to the cathode when applying 200 mA cm^{-2}. This finding aligns with the enhanced HER observed at this current density, both in this study (Figures 2a) and in previous reports,[14,36] suggesting that increased water diffusion is driven by electro–osmotic drag.

X–ray Photoelectron Spectroscopy (XPS) analysis was conducted to assess the elemental chemical composition at the surface of the electrodes before and after the eCO_2R (Table S4). C 1*s* spectra of the GDE before eCO_2R exhibit a dominant contribution from sp^2–hybridized C = C bond (284.5 eV), followed by Bi–C (283.2 eV), and a π–π^* shake–up transition at 290.9 eV (Figure S10a).[54,55] After eCO_2R, a new peak emerged at 287.5 eV, which can be attributed to CO_3^{2-} and suggests the presence of carbonate on the GDE surface after eCO_2R (Figure S10b). C 1*s* spectra of the nickel mesh shows new signals at 289.3 and 291.1 eV, assigned to carbonate (CO_3^{2-}) and bicarbonate (HCO_3^-), respectively (Figure S10d). As the electrolyzer employs an AEM, the anionic species produced at the cathode (CO_3^{2-} and HCO_3^-) migrate across the membrane and can observed on the nickel anode surface. K 2*p* was identified after eCO_2R for the GDE —$2p_{3/2}$ (290.9 eV) and $2p_{1/2}$ (293.7 eV)— and the nickel mesh—$2p_{3/2}$ (293.6 eV) and $2p_{1/2}$ (296.4 eV) (Figure S10b–S10d).[54,55] Potassium presence on the GDE supports the hypothesis that K^+ ions migrate from the anode during operation. A well–separated doublet (Δ= 5.31 eV) is observed in the Bi 4*f* GDE spectra before eCO_2R, indicating the presence of both Bi^0 and Bi^{3+} species (Figure 6a). After eCO_2R, the spectra maintained the profile, however, all the signals shifted toward lower binding energies (Figure 6b), indicating an increase in electron density around the Bi atoms, which could be induced by the presence of the carbonate species.[28,54] The Ni $2p_{3/2}$ spectra before eCO_2R shows a mixture of nickel species (Ni^{2+} and Ni^0) (Figure 6c). The major contribution was attributed to $Ni(OH)_2$, followed by Ni^0, and NiO species.[54,56,57] After eCO_2R, all signals exhibited a shift toward higher binding energies (Figure 6d), which confirms nickel oxidation during OER.[57–59]

The X–ray diffraction patterns of the pristine material (Figure S11a) revealed characteristic peaks of tetragonal β–Bi_2O_3, along with additional signals attributed to monoclinic α– Bi_2O_3, and Bi^0, indicating a mixed–phase composition.

https://doi.org/10.1021/acssuschemeng.5c11134
ACS Sustainable Chem. Eng. 2026, 14, 1608–1619

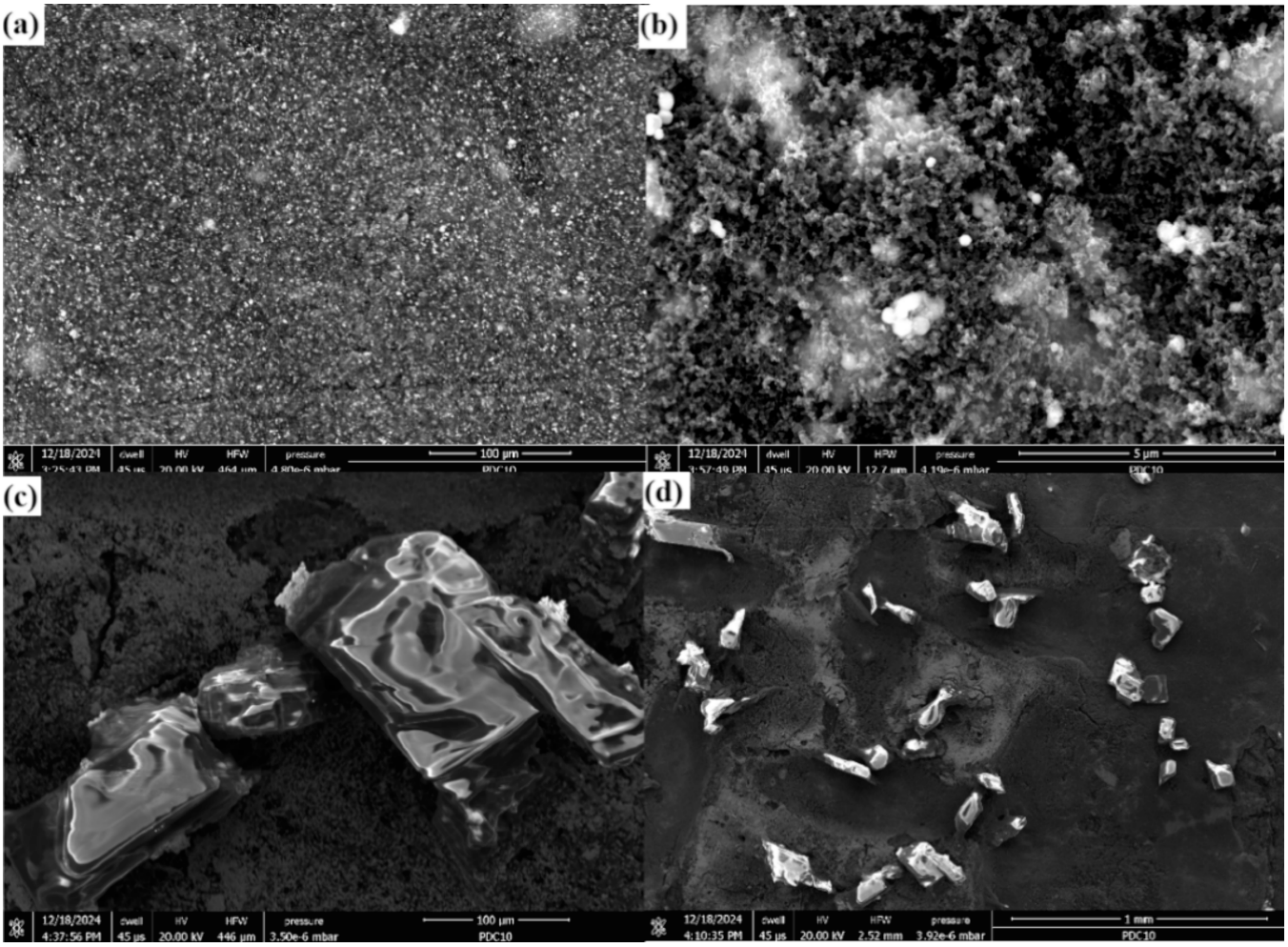

Figure 5. Pristine cathodic GDE before eCO_2R using different magnifications: (a) 100 and (b) 5 μm. Cathodic GDE after eCO_2R different magnifications: (c) 100 μm and (d) 1 mm.

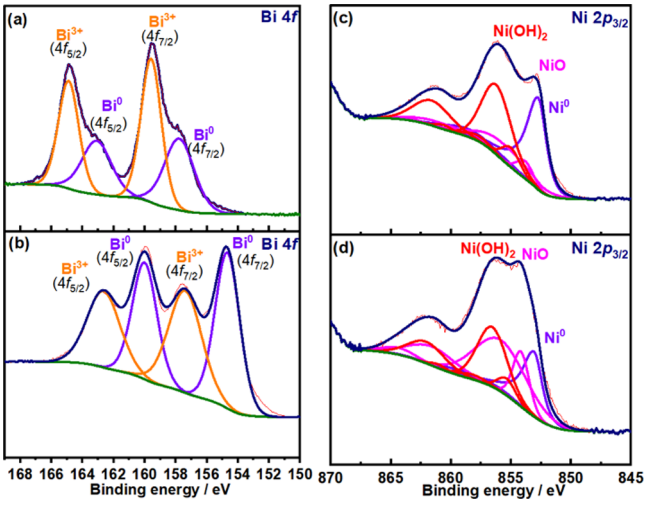

Figure 6. XPS spectra for the GDE in the core level Bi 4*f* (a) before eCO_2R and (b) after eCO_2R. XPS spectra for the Ni mesh in the core level Ni 2*p* (c) before eCO_2R and (d) after eCO_2R.

After CO_2 electrolysis (Figure S11b), new peaks corresponding to $Bi_2O_2CO_3$, K_2CO_3, and $KHCO_3$ appeared.

An Inductively Coupled Plasma Mass Spectrometry (ICP–MS) analysis was conducted on the anolyte after 2 h of eCO_2R at 200 mA cm^{-2} to assess the potential nickel leaching from the nickel mesh (Table 2). No significant leaching was detected, indicating that the nickel mesh remains stable and confirming its robustness as a material for CO_2 electrolysis to formate under the alkaline conditions applied in this study.

Table 2. ICP–MS Results of the Anolyte (1 M KOH) before the Reaction and after the Reaction, Applying 200 mA cm^{-2}[a]

	Ni	
sample	[ ]/μg/L	SD/μg/L
1 M KOH before eCO_2R	44.689	5.336
1 M KOH after eCO_2R	58.696	4.669

[a]The concentration ([ ]) of nickel is presented with the SD.

3.5. Techno–Economic Studies for Industrial Viability

A techno–economic analysis (TEA) assessed the viability of the ZG electrolyzer to economies of scale. The analysis was based on optimal experimental results obtained in this study at 50 mA cm^{-2} using the nickel mesh (70.37% FE, 2.16 V, 3.48 kWh kg^{-1}, and 0.555 M formate) and the IrO_2–based electrode (45.55% FE, 2.16 V, 5.13 kWh kg^{-1}, and 0.158 M formate) (Table S5). The economic performance was analyzed based on the levelized cost of formic acid (LCFA) from the

https://doi.org/10.1021/acssuschemeng.5c11134
ACS Sustainable Chem. Eng. 2026, 14, 1608–1619

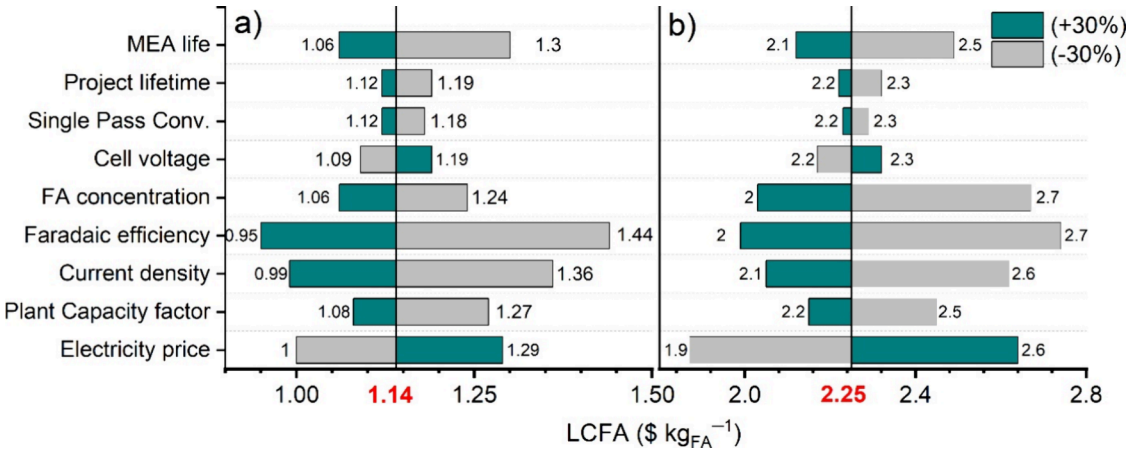

Figure 7. Sensitivity analysis of the calculated levelized cost of formic acid (LCFA) in the eCO$_2$R to formate process using a ZG reactor with an (a) anodic nickel mesh and (b) anodic iridium−based catalysts. Baseline electrochemistry parameters originate from the optimal experimental results with a nickel mesh and iridium−based catalysts (Table S5) and operating assumptions of Table S5.

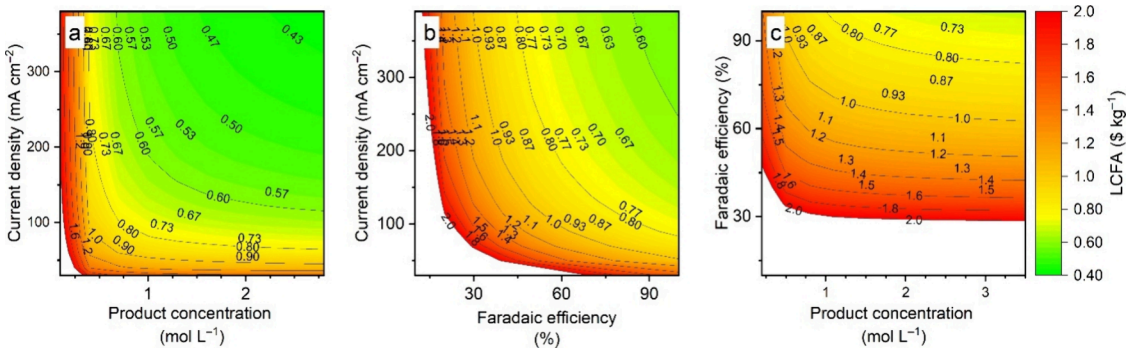

Figure 8. Contour plots depicting the combined effect of two independent electrochemical performance parameters on the LCFA: (a) current density and formate concentration, (b) current density and faradaic efficiency, and (c) faradaic efficiency and product concentration. The rest of the baseline electrochemistry parameters stem from the optimal experimental results with a nickel catalyst (Table S5) and operating assumptions of Table S6.

perspective of an industrial−scale formic acid production system, as modeled in our previous study.[4] This considers a CO_2 electrolysis reactor model composed of 50 stacks of 200 zero−gap cells with an active surface area of 0.6 m^2, i.e., a reactor with a total active surface area of 6,000 m^2 adapted for the use of either nickel or iridium as catalytic metal, as well as its entire balance of plant (BoP). Next, a pressure swing adsorption (PSA) systems[60] envisaged for the separation and recycling of unreacted CO_2.[60] Finally, a liquid−liquid separation unit designed for extracting and purifying formic acid to a commercial concentration (>85 wt %) is considered. This involves acidifying the formate solution before it is introduced into the separation system, where the formic acid is purified by azeotropic distillation.[61−63] The capital costs relating to the electrolysis unit (stacks and BoP) were calculated from the component costs in relation to their quantities,[64] while the extra operational cost related to acidification of formate was considered in process consumables, assumed to represent 2.5% of the initial investment on a yearly basis or a contribution to the total LCFA, which amounts to \$0.06 kg$_{FA}^{-1}$ (Figure S13). For the PSA and product separation units, their costs were derived from existing models[60,63] and updated to the implemented flows (materials and energy), following a comprehensive methodology.[4] The analysis of the influence of various technical and economic parameters on the LCFA in this specific scenario is summarized in Figure 7.

A moderate single−pass conversion of 15% was assumed, considering the CO_2 excess applied to the 6,000 m^2 reactor with an active area of 0.6 m^2/cell. This excess is required to avoid the depletion of CO_2 along the flow resulting from a high conversion rate (50−60% as commonly assumed in TEAs),[65] causing a substantial deterioration not only in Faradaic efficiency of the target product, but also in the current density due to mass transport losses. More information regarding the effect of the single−pass conversion on these electrochemical parameters is given as contour plots in Figures S12a-12c. Applying the operation baseline assumptions specified in Table S6, the nickel mesh yields a price of \$1.14 kg$_{FA}^{-1}$. This price is more favorable than the results obtained using an IrO_2−based anode (\$2.25 kg$_{FA}^{-1}$) due to the worse electrochemical performance in the production of formate (Table S5) and the greater economic impact of product purification. Sensitivity analyses (Figure 7) show a substantial dependency on specific operating parameters (plant capacity factor, MEA lifetime, and electricity price) and electrochemical performance indicators (product concentration, faradaic efficiency, and current density). To interpret the ± 30% sensitivity analysis in Figure 7a, a + 30% increase in current density (i.e., operating at 65.0 mA cm^{-2}) using the nickel anode, while maintaining the rest of the parameters constant (Table S5, S6), would result in an

https://doi.org/10.1021/acssuschemeng.5c11134
ACS Sustainable Chem. Eng. 2026, 14, 1608−1619

LCFA of \$0.99 kg_{FA}^{-1}. A more comprehensive analysis focused on electrochemical performance using exclusively nickel as anode is presented in contour plots, illustrating the combined effects of current density and product concentration (Figure 8a), current density and faradaic efficiency (Figure 8b), and faradaic efficiency and product concentration (Figure 8c) on the LCFA value. Herein, green color highlights economic competition with established industrial processes (\$0.65 kg_{FA}^{-1}). Among the electrochemical performance indicators, current density and product concentration are the most important in the ZG configuration studied in this work, as observed in the extended green color in Figure 8a.

TEA studies suggest a promising economic outlook for scaling up formic acid production to an industrial level using the proposed ZG electrolyzer when nickel is used instead of iridium as the anode catalyst. This advantage stems from nickel's low cost and minimal activity in FOR, in contrast to iridium's high cost. However, reaching the target market of \$0.6 kg_{FA}^{-1} will require further technological improvements to enable operation at current densities higher than 150 mA cm^{-2} and product concentration above 1.5 M (Figure 8a). Further contours plot analyses assessing the combined impact of influential operating parameters (single−pass conversion, electricity price, and plant capacity factor) and electrochemical performance indicators (current density, product concentration, and faradaic efficiency) on the LCFA (as observed in Figure 8) confirmed the requirement of operating at higher current densities (Figures S12a and S12d), considering that at least the target product concentration of 0.555 M is achieved, to implement this ZG configuration for industrial scalability. Furthermore, this technology could benefit from the availability of lower−cost renewable energy sources, such as onshore wind and utility−scale photovoltaics, compared to the electricity price assumed in this study (¢4.5 kWh^{-1}) (Figures S12d-S12f).[66]

4. CONCLUSIONS

This study demonstrates the viability of replacing IrO_2 with a nickel mesh anode for the eCO_2R−to−formate under alkaline conditions in a zero−gap electrolyzer using an AEM configuration. Nickel is not only an abundant metal, but it also exhibits excellent stability and selectivity toward formate production in the tested conditions. The nickel mesh anode resulted in the highest formate concentration reported to date for this type of electrolyzer configuration (0.555 M), along with reduced energy consumption (3.48 kWh $kg_{formate}^{-1}$). In contrast, the IrO_2−based anode underperformed across all studied current densities, showing lower faradaic efficiencies and higher energy consumption to formate, thus proving detrimental to the eCO_2RR−to−formate in this reactor configuration. The effect of the anolyte was also investigated. While the nature of the cation showed minimal influence on the cell performance, the identity of the anion had a significant impact, especially in the anodic reaction due to its effect on pH. Our investigation suggests that on the nickel mesh anode, the OER becomes less favorable under neutral conditions due to increased competition with the FOR. Therefore, operating in an alkaline environment is essential to both thermodynamically and kinetically favor the OER on the nickel anode. *Post mortem* electrode characterization using SEM, XPS, and XRD revealed the presence of potassium carbonate on the GDE surface, along with an increase of reduced Bi^0 (cathode) and oxidized $NiO/Ni(OH)_2$ (anode) species during operation. ICP−MS analyses showed no sign of nickel leaching into the anolyte, indicating the stability of the nickel mesh. Techno−economic analyses demonstrate the improved economic viability of the ZG configuration with the nickel mesh, emphasizing the need for further cell development to enhance eCO_2R selectivity to formate at high current densities for achieving economic competition at the industrial scale.

■ ASSOCIATED CONTENT

Supporting Information

The Supporting Information is available free of charge at https://pubs.acs.org/doi/10.1021/acssuschemeng.5c11134.

Additional experimental data and figures related to the discussion of results, including representative examples from the literature of eCO_2R to formate, pictures of the zero-gap cell components and experimental setup, additional electrochemical performance plots and tables, SEM and EDS mapping analyses, XPS and XRD characterization, and supplementary details on the techno-economic analysis (TEA) (PDF)

■ AUTHOR INFORMATION

Corresponding Authors

Andreyna Ferreira Gamba − *Institute of Energy Technologies, Fundamental Electrochemistry (IET−1), Forschungszentrum Jülich, Jülich 52425, Germany; Institute of Physical Chemistry, RWTH Aachen University, Aachen 52062, Germany;* orcid.org/0009-0000-5072-6174; Email: a.gamba@fz-juelich.de

Sergio Sanz − *Institute of Energy Technologies, Fundamental Electrochemistry (IET−1), Forschungszentrum Jülich, Jülich 52425, Germany*; Email: s.calvo@fz-juelich.de

Authors

Urbain Nzotcha − *Institute of Energy Technologies, Fundamental Electrochemistry (IET−1), Forschungszentrum Jülich, Jülich 52425, Germany*

Hermann Tempel − *Institute of Energy Technologies, Fundamental Electrochemistry (IET−1), Forschungszentrum Jülich, Jülich 52425, Germany;* orcid.org/0000-0002-9794-6403

Rüdiger−A. Eichel − *Institute of Energy Technologies, Fundamental Electrochemistry (IET−1), Forschungszentrum Jülich, Jülich 52425, Germany; Institute of Physical Chemistry and Faculty of Mechanical Engineering, RWTH Aachen University, Aachen 52062, Germany;* orcid.org/0000-0002-0013-6325

Complete contact information is available at: https://pubs.acs.org/10.1021/acssuschemeng.5c11134

Author Contributions

S.S., H.T., A.F.G., and R.E. conceived the idea. A.F.G. collected and analyzed the data. S.S. and A.F.G. interpreted the data. U.N. performed techno−economic analyses. All authors contributed to the writing and editing of the manuscript.

Notes

The authors declare no competing financial interest.

https://doi.org/10.1021/acssuschemeng.5c11134
ACS Sustainable Chem. Eng. 2026, 14, 1608−1619

■ ACKNOWLEDGMENTS

We thank the financial support from the German Federal Ministry of Research, Technology, and Space within the projects: "iNEW2.0——Inkubator Nachhaltige Elektrochemische Wertschöpfungsketten" Project No. 03SF0627A and "PHOENIX − Launch Space Power−to−X" Project No. 03SF0775A. We thank Dr. Heinrich Hartmann, Forschungszentrum Jülich GmbH (IET−4), for the XPS measurements.

■ REFERENCES

(1) Hashimoto, K. *Global Carbon Dioxide Recycling: For Global Sustainable Development by Renewable Energy*, 1st ed.; Springer, 2019.
(2) Bui, M.; Adjiman, C. S.; Bardow, A.; Anthony, E. J.; Boston, A.; Brown, S.; Fennell, P. S.; Fuss, S.; Galindo, A.; Hackett, L. A.; Hallett, J. P.; Herzog, H. J.; Jackson, G.; Kemper, J.; Krevor, S.; Maitland, G. C.; Matuszewski, M.; Metcalfe, I. S.; Petit, C.; Puxty, G.; Reimer, J.; Reiner, D. M.; Rubin, E. S.; Scott, S. A.; Shah, N.; Smit, B.; Trusler, J. P. M.; Webley, P.; Wilcox, J.; Mac Dowell, N. Carbon Capture and Storage (CCS): The Way Forward. *Energy Environ. Sci.* **2018**, *11* (5), 1062−1176.
(3) Lee, H.; Kwon, S.; Park, N.; Cha, S. G.; Lee, E.; Kong, T. H.; Cha, J.; Kwon, Y. Scalable Low-Temperature CO_2 Electrolysis: Current Status and Outlook. *JACS Au* **2024**, *4* (9), 3383−3399.
(4) Nzotcha, U.; Sanz, S.; Tempel, H.; Eichel, R. Techno-Economic Perspective on the Electroreduction of CO_2 to Formic Acid: Scale-up Strategies towards Industrial Viability. *Angew. Chemie - Int. Ed.* **2025**, *64* (31), No. e202418114.
(5) Jovanovic, S.; Jakes, P.; Merz, S.; Daniel, D. T.; Eichel, R. A.; Granwehr, J. In Operando NMR Investigations of the Aqueous Electrolyte Chemistry during Electrolytic CO_2 Reduction. *Commun. Chem.* **2023**, *6* (1), 268.
(6) Fernández-Caso, K.; Díaz-Sainz, G.; Alvarez-Guerra, M.; Irabien, A. Electroreduction of CO_2: Advances in the Continuous Production of Formic Acid and Formate. *ACS Energy Lett.* **2023**, *8* (4), 1992−2024.
(7) Zhang, C.; Hao, X.; Wang, J.; Ding, X.; Zhong, Y.; Jiang, Y.; Wu, M.; Long, R.; Gong, W.; Liang, C.; Cai, W.; Low, J.; Xiong, Y. Concentrated Formic Acid from CO_2 Electrolysis for Directly Driving Fuel Cell. *Angew. Chemie - Int. Ed.* **2024**, *63* (13), No. e202317628.
(8) Lin, J.; Chi, H.; Liu, H.; Fan, Q.; Yan, T.; Kuang, S.; Wang, H.; Li, M.; Yan, Y.; Zhang, T.; Zhang, S.; Ma, X. Concentrated Formate Produced through Co-Electrolysis of CO_2 and Methanol in a Zero-Gap Electrolyzer. *AIChE J.* **2024**, *70* (5), No. e18382.
(9) Lin, J.; Zhang, Y.; Xu, P.; Chen, L. CO_2 Electrolysis: Advances and Challenges in Electrocatalyst Engineering and Reactor Design. *Mater. Reports Energy* **2023**, *3* (2), No. 100194.
(10) Schuler, E.; Morana, M.; Ermolich, P. A.; Lüschen, K.; Greer, A. J.; Taylor, S. F. R.; Hardacre, C.; Shiju, N. R.; Gruter, G. J. M. Formate as a Key Intermediate in CO_2 Utilization. *Green Chem.* **2022**, *24* (21), 8227−8258.
(11) Kirner, J.; Chen, Y.; Liu, H.; Song, J.; Liao, J.; Li, W.; Zhao, F. Exploring Electrochemical Flow-Cell Designs and Parameters for CO_2 Reduction to Formate under Industrially Relevant Conditions. *J. Electrochem. Soc.* **2022**, *169* (5), No. 054511.
(12) Vo, T.; Purohit, K.; Nguyen, C.; Biggs, B.; Mayoral, S.; Haan, J. L. Formate: An Energy Storage and Transport Bridge between Carbon Dioxide and a Formate Fuel Cell in a Single Device. *ChemSusChem* **2015**, *8* (22), 3853−3858.
(13) Zou, J.; Liang, G.; Lee, C. Y.; Wallace, G. G. Progress and Perspectives for Electrochemical CO_2 Reduction to Formate. *Mater. Today Energy* **2023**, *38*, No. 101433.
(14) Sassenburg, M.; Kelly, M.; Subramanian, S.; Smith, W. A.; Burdyny, T. Zero-Gap Electrochemical CO_2 Reduction Cells: Challenges and Operational Strategies for Prevention of Salt Precipitation. *ACS Energy Lett.* **2023**, *8* (1), 321−331.
(15) Xia, C.; Zhu, P.; Jiang, Q.; Pan, Y.; Liang, W.; Stavitski, E.; Alshareef, H. N.; Wang, H. Continuous Production of Pure Liquid Fuel Solutions via Electrocatalytic CO_2 Reduction Using Solid-Electrolyte Devices. *Nat. Energy* **2019**, *4* (9), 776−785.
(16) Guo, J.; Qi, W.; Mo, R.; Yuan, F.; Wang, L.; Li, Y. A Tunable Strategy for Continuous Production of Electrolyte-Free Formic Acid and Sodium Formate in a Solid-State-Electrolyte Based Electrocatalytic CO_2 Reduction System. *Adv. Sci.* **2025**, *12* (36), No. e08152.
(17) Rutjens, B.; von Foerster, K.; Schmid, B.; Weinrich, H.; Sanz, S.; Tempel, H.; Eichel, R. A. Impact of the PiperION Anion Exchange Membrane Thickness on the Performance of a CO_2-to-HCOOH Three-Compartment Electrolyzer. *Ind. Eng. Chem. Res.* **2024**, *63* (9), 3986−3996.
(18) Duarte, M.; Hereijgers, J.; Daems, N.; Van Daele, S.; Breugelmans, T. The Importance of Target Product Engineering for Long-Term Operation of CO_2 Zero-Gap Electrolysers. *J. Environ. Chem. Eng.* **2022**, *10* (3), No. 107836.
(19) Nomoto, K.; Okazaki, T.; Beppu, K.; Shishido, T.; Amano, F. Highly Selective Formate Formation via Bicarbonate Conversions. *EES Catal.* **2024**, *2*, 1277−1284.
(20) Li, T.; Lees, E. W.; Zhang, Z.; Berlinguette, C. P. Conversion of Bicarbonate to Formate in an Electrochemical Flow Reactor. *ACS Energy Lett.* **2020**, *5*, 2624−2630.
(21) Zhang, Z.; Xi, D.; Ren, Z.; Li, J. A Carbon-Efficient Bicarbonate Electrolyzer. *Cell Reports Phys. Sci.* **2023**, *4*, No. 101662.
(22) Saha, P.; Henckel, D.; Baez-Cotto, C.; Intia, F.; Hu, L.; Van Cleve, T.; Neyerlin, K. C. Anolyte Enhances Catalyst Utilization and Ion Transport Inside a CO_2 Electrolyzer Cathode. *J. Electrochem. Soc.* **2023**, *170* (1), No. 014505.
(23) Hu, L.; Wrubel, J. A.; Baez-Cotto, C. M.; Intia, F.; Park, J. H.; Kropf, A. J.; Kariuki, N.; Huang, Z.; Farghaly, A.; Amichi, L.; Saha, P.; Tao, L.; Cullen, D. A.; Myers, D. J.; Ferrandon, M. S.; Neyerlin, K. C. A Scalable Membrane Electrode Assembly Architecture for Efficient Electrochemical Conversion of CO_2 to Formic Acid. *Nat. Commun.* **2023**, *14*, 7605.
(24) Jiang, H.; Wang, L.; Gao, B.; Li, Y.; Guo, Y.; Zhuo, M.; Sun, K.; Lu, B.; Jia, M.; Yu, X.; Wang, H.; Li, Y. The Anolyte Matters: Towards Highly Efficient Electrochemical CO_2 Reduction. *Chem. Eng. J.* **2021**, *422*, No. 129923.
(25) Vass, Á.; Endrődi, B.; Samu, G. F.; Balog, Á.; Kormányos, A.; Cherevko, S.; Janáky, C. Local Chemical Environment Governs Anode Processes in CO_2 Electrolyzers. *ACS Energy Lett.* **2021**, *6* (11), 3801−3808.
(26) Masel, R. I.; Liu, Z.; Yang, H.; Kaczur, J. J.; Carrillo, D.; Ren, S.; Salvatore, D.; Berlinguette, C. P. An Industrial Perspective on Catalysts for Low-Temperature CO_2 Electrolysis. *Nat. Nanotechnol.* **2021**, *16* (2), 118−128.
(27) Belsa, B.; Xia, L.; Golovanova, V.; Polesso, B.; Pinilla-Sánchez, A.; San Martín, L.; Ye, J.; Dinh, C. T.; García de Arquer, F. P. Materials Challenges on the Path to Gigatonne CO_2 Electrolysis. *Nat. Rev. Mater.* **2024**, *9* (8), 535−549.
(28) Mouler, J. F.; Stickle, W. F.; Sobol, P. E.; Bomben, K. D. *Handbook of X-Ray Photoelectron Spectroscopy*; Perkin-Elmer Corporation. Physical Electronics Division, 1992.
(29) Liu, W.; Wang, K. Recent Development of Non-Noble Metal Catalysts for Oxygen Evolution Reaction (OER) under Different PH. *React. Chem. Eng.* **2025**, *10* (8), 1704−1729.
(30) Flores-Lasluisa, J. X.; Huerta, F.; Cazorla-Amorós, D.; Morallón, E. Transition Metal Oxides with Perovskite and Spinel Structures for Electrochemical Energy Production Applications. *Environ. Res.* **2022**, *214*, No. 113731.
(31) Chen, X.; Yu, X.; Yang, C.; Wang, G. Enhancing OER and Overall Water Splitting Performance of Amorphous NiFe LDH Grown on Ni Foam with the Needle-like NiCoP Transition Layer. *J. Solid State Chem.* **2024**, *333*, No. 124649.
(32) Lyu, X.; Li, J.; Jafta, C. J.; Bai, Y.; Canales, C. P.; Magnus, F.; Ingason, S.; Serov, A. Investigation of Oxygen Evolution Reaction with Ni Foam and Stainless-Steel Mesh Electrodes in Alkaline Seawater Electrolysis. *J. Environ. Chem. Eng.* **2022**, *10*, No. 108486.
(33) Stevens, M. B.; Trang, C. D. M.; Enman, L. J.; Deng, J.; Boettcher, S. W. Reactive Fe-Sites in Ni/Fe (Oxy)Hydroxide Are

https://doi.org/10.1021/acssuschemeng.5c11134
ACS Sustainable Chem. Eng. 2026, 14, 1608−1619

Responsible for Exceptional Oxygen Electrocatalysis Activity. *J. Am. Chem. Soc.* **2017**, *139* (33), 11361−11364.
(34) Díaz-Sainz, G.; Fernández-Caso, K.; Lagarteira, T.; Delgado, S.; Alvarez-Guerra, M.; Mendes, A.; Irabien, A. Coupling Continuous CO_2 Electroreduction to Formate with Efficient Ni-Based Anodes. *J. Environ. Chem. Eng.* **2023**, *11*, No. 109171.
(35) El-Nagar, G. A.; Haun, F.; Gupta, S.; Stojkovikj, S.; Mayer, M. T. Unintended Cation Crossover Influences CO_2 Reduction Selectivity in Cu-Based Zero-Gap Electrolysers. *Nat. Commun.* **2023**, *14* (1), 2062.
(36) Simonson, H.; Henckel, D.; Klein, W. E.; Neyerlin, K. C.; Smith, W. A. Cation Crossover Limits Accessible Current Densities for Zero-Gap Alkaline CO_2 Reduction to Ethylene. *ACS Sustain. Chem. Eng.* **2025**, *13* (2), 823−833.
(37) Ma, M.; Zheng, Z.; Yan, W.; Hu, C.; Seger, B. Rigorous Evaluation of Liquid Products in High-Rate CO_2/CO Electrolysis. *ACS Energy Lett.* **2022**, *7* (8), 2595−2601.
(38) Xu, Q.; Liu, S.; Longhin, F.; Kastlunger, G.; Chorkendorff, I.; Seger, B. Impact of Anodic Oxidation Reactions in the Performance Evaluation of High-Rate CO_2/CO Electrolysis. *Adv. Mater.* **2024**, *36* (2), No. 2306741.
(39) Xu, Q.; Xu, A.; Garg, S.; Moss, A. B.; Chorkendorff, I.; Bligaard, T.; Seger, B. Enriching Surface-Accessible CO_2 in the Zero-Gap Anion-Exchange-Membrane-Based CO_2 Electrolyzer. *Angew. Chemie - Int. Ed.* **2023**, *62* (3), No. e202214383.
(40) Larrazábal, G. O.; Strøm-Hansen, P.; Heli, J. P.; Zeiter, K.; Therkildsen, K. T.; Chorkendorff, I.; Seger, B. Analysis of Mass Flows and Membrane Cross-over in CO_2 Reduction at High Current Densities in an MEA-Type Electrolyzer. *ACS Appl. Mater. Interfaces* **2019**, *11* (44), 41281−41288.
(41) Zhong, X.; Peng, H. J.; Xia, C.; Liu, X. Electrolyte Effect on Electrochemical CO_2 Reduction to Multicarbon Products. *J. Phys. Chem. C* **2024**, *128* (9), 3621−3631.
(42) Qin, X.; Hansen, H. A.; Honkala, K.; Melander, M. M. Cation-Induced Changes in the Inner- and Outer-Sphere Mechanisms of Electrocatalytic CO_2 Reduction. *Nat. Commun.* **2023**, *14*, 7607.
(43) Petrov, K. V.; Koopman, C. I.; Subramanian, S.; Koper, M. T. M.; Burdyny, T.; Vermaas, D. A. Bipolar Membranes for Intrinsically Stable and Scalable CO_2 Electrolysis. *Nat. Energy* **2024**, *9*, 932−938.
(44) Liao, W. C.; Tsai, D. H.; Hong, W. Z.; Huang, Y. H.; Lin, L. C.; Pan, Y. T. Enabling Direct CO_2 Electrolysis by Alkali Metal Cation Substituted Membranes in a Gas Diffusion Electrode Reactor. *Chem. Eng. J.* **2022**, *434*, No. 1347657.
(45) Garg, S.; Giron Rodriguez, C. A.; Rufford, T. E.; Varcoe, J. R.; Seger, B. How Membrane Characteristics Influence the Performance of CO_2 and CO Electrolysis. *Energy Environ. Sci.* **2022**, *15*, 4440−4469.
(46) Ewis, D.; Arsalan, M.; Khaled, M.; Pant, D.; Ba-Abbad, M. M.; Amhamed, A.; El-Naas, M. H. Electrochemical Reduction of CO_2 into Formate/Formic Acid: A Review of Cell Design and Operation. *Sep. Purif. Technol.* **2023**, *316*, No. 123811.
(47) Abarca, J. A.; Díaz-Sainz, G.; Irabien, A. Inhibiting Salt Precipitation on the Gas Diffusion Electrode Surface in Gas-Phase CO_2 Electroreduction to Formate by Using an Acidic Anolyte. *J. CO2 Util.* **2024**, *86*, No. 102897.
(48) Abarca, J. A.; Abdolhosseini, G.; Sanz, J. M.; Solla-Gullón, J.; Garcés-Pineda, F. A.; Díaz-Sainz, G.; Irabien, A. Coupling Ni-Based Anodes for Textile Industry Process Stream Electrooxidation with Electrocatalytic CO_2 Reduction to Formate in Gas Phase. *J. CO2 Util.* **2025**, *93*, No. 103053.
(49) Hosseini-Benhangi, P.; Gyenge, C. C.; Gyenge, E. L. The Carbon Dioxide Redox Flow Battery: Bifunctional CO_2 Reduction/Formate Oxidation Electrocatalysis on Binary and Ternary Catalysts. *J. Power Sources* **2021**, *495*, No. 229752.
(50) Fujita, E.; Muckerman, J. T.; Himeda, Y. Interconversion of CO_2 and Formic Acid by Bio-Inspired Ir Complexes with Pendent Bases. *Biochim. Biophys. Acta - Bioenerg.* **2013**, *1827*, 1031−1038.
(51) McCallum, C.; Gabardo, C. M.; O'Brien, C. P.; Edwards, J. P.; Wicks, J.; Xu, Y.; Sargent, E. H.; Sinton, D. Reducing the Crossover of Carbonate and Liquid Products during Carbon Dioxide Electroreduction. *Cell Reports Phys. Sci.* **2021**, *2*, No. 100522.
(52) Hasa, B.; Cherniack, L.; Xia, R.; Tian, D.; Ko, B. H.; Overa, S.; Dimitrakellis, P.; Bae, C.; Jiao, F. Benchmarking Anion-Exchange Membranes for Electrocatalytic Carbon Monoxide Reduction. *Chem. Catal.* **2023**, *3*, No. 100450.
(53) Reyes, A.; Jansonius, R. P.; Mowbray, B. A. W.; Cao, Y.; Wheeler, D. G.; Chau, J.; Dvorak, D. J.; Berlinguette, C. P. Managing Hydration at the Cathode Enables Efficient CO_2/CO Electrolysis at Commercially Relevant Current Densities. *ACS Energy Lett.* **2020**, *5*, 1612−1618.
(54) Wagner, C. D. NIST X-Ray Photoelectron Spectrometry Database. *NIST Stand. Ref. Database* **1991**, 1−76.
(55) Caracciolo, L.; Madec, L.; Martinez, H. XPS Analysis of K-Based Reference Compounds to Allow Reliable Studies of Solid Electrolyte Interphase in K-Ion Batteries. *ACS Appl. Energy Mater.* **2021**, *4* (10), 11693−11699.
(56) Martínez, J.; Mosquera-Vargas, E.; Fuenzalida, V.; Flores, M.; Bolaños, G.; Diosa, J. Surface and Electrical Characterization of Bilayers Based on $BiFeO_3$ and VO_2. *Nanomaterials* **2022**, *12* (15), 2578.
(57) Blume, A. R.; Calvet, W.; Ghafari, A.; Mayer, T.; Knop-Gericke, A.; Schlögl, R. Structural and Chemical Properties of NiO_x Thin Films: The Role of Oxygen Vacancies in NiOOH Formation in a H_2O Atmosphere. *Phys. Chem. Chem. Phys.* **2023**, *25* (37), 25552−25565.
(58) Plevová, M.; Hnát, J.; Bouzek, K. Electrocatalysts for the Oxygen Evolution Reaction in Alkaline and Neutral Media. A Comparative Review. *J. Power Sources* **2021**, *507*, No. 230072.
(59) Sadiek, I. M.; Mohammad, A. M.; El-Shakre, M. E.; El-Deab, M. S. Electrocatalytic Activity of Nickel Oxide Nanoparticles-Modified Electrodes: Optimization of the Loading Level and Operating pH towards the Oxygen Evolution Reaction. *Int. J. Hydrogen Energy* **2012**, *37* (1), 68−77.
(60) Jouny, M.; Luc, W.; Jiao, F. General Techno-Economic Analysis of CO_2 Electrolysis Systems. *Ind. Eng. Chem. Res.* **2018**, *57* (6), 2165−2177.
(61) Ramdin, M.; Morrison, A. R. T.; de Groen, M.; van Haperen, R.; de Kler, R.; Irtem, E.; Laitinen, A. T.; van den Broeke, L. J. P.; Breugelmans, T.; Trusler, J. P. M.; Jong, W. d.; Vlugt, T. J. H. High-Pressure Electrochemical Reduction of CO_2 to Formic Acid/Formate: Effect of PH on the Downstream Separation Process and Economics. *Ind. Eng. Chem. Res.* **2019**, *58*, 22718−22740.
(62) Wang, X.; Fu, H.; Du, D.; Zhou, Z.; Zhang, A.; Su, C.; Ma, K. The Comparison of pKa Determination between Carbonic Acid and Formic Acid and Its Application to Prediction of the Hydration Numbers. *Chem. Phys. Lett.* **2008**, *460*, 339−342.
(63) Ramdin, M.; De Mot, B.; Morrison, A. R. T.; Breugelmans, T.; Van Den Broeke, L. J. P.; Trusler, J. P. M.; Kortlever, R.; De Jong, W.; Moultos, O. A.; Xiao, P.; Webley, P. A.; Vlugt, T. J. H. Electroreduction of CO_2/CO to C_2 Products: Process Modeling, Downstream Separation, System Integration, and Economic Analysis. *Ind. Eng. Chem. Res.* **2021**, *60* (49), 17862−17880.
(64) Battelle Memorial Institute *Manufacturing Cost Analysis of PEM Fuel Cell Systems for 5- and 10-KW Backup Power Applications* 2016
(65) Shin, H.; Hansen, K. U.; Jiao, F. Techno-Economic Assessment of Low-Temperature Carbon Dioxide Electrolysis. *Nat. Sustain.* **2021**, *4* (10), 911−919.
(66) Kost, C.; Shammugam, S.; Fluri, V.; Peper, D.; Memar, A. D.; Schlegel, T. *Levelized Cost of Electricity- Renewable Energy Technologies* 2021

https://doi.org/10.1021/acssuschemeng.5c11134
ACS Sustainable Chem. Eng. 2026, 14, 1608−1619